Supporting Information

SI Materials and Methods

Medicago sterilization and germination.

Unbroken wild type A17 *Medicago truncatula* seeds are collected and scarified by immersing them in concentrated sulphuric acid H_2SO_4 for 10 min. To ensure that the samples are sterile, the scarified seeds are soaked in 10% bleach solution (10% bleach in 0.1% Tween 20; the bleach contains 6% sodium hypochlorite) with gentle agitation in laminar flow for 10 min. For imbibition, the seeds are first placed in sterile distilled water and left on a shaker for 3 hours. Subsequently, the seeds are incubated at 4°C for 26 hours. Finally, the seeds are transferred to a petri dish and incubated at 28°C for 18 hours. Petri dishes are inverted to encourage growth of straight radicles before transplanting into a transparent growth chamber. These imbibition and incubation steps are done in unlit conditions. Between all steps, sterile distilled water is used to decant the seeds. This protocol is performed to ensure synchronized germination (see reference [31] of main text for further information).

Fahraeus media and Gelzan preparation.

Root growth experiments were carried out with *Medicago* plants grown in a Fahraeus media (F-media) hydrogel. The F-media consisted of: 0.9 mM $CaCl_2$; 0.5 mM $MgSO_4$; 20 µM KH_2PO_4; 10 µM Na_2HPO_4; 20 µM ferric citrate; 1.0 mM NH_4NO_3; 33 µg/L $MnCl_2$; 33 µg/L $CuSO_4$; 7 µg/L $ZnSO_4$*$7H_2O$; 100 µg/L H_3BO_3; 33 µg/L Na_2MoO_4; 218 mg/L MES free acid monohydrate; and 2.5 g/L Gelrite (Sigma-Aldrich) dissolved in distilled water. The gel solution was autoclaved before solidifying to ensure sterile conditions (see reference [31] of main text for further information). To create a mechanical barrier, a glass slide of appropriate length was inserted into a Magenta box (Magenta Corp.). The liquid F-media was then poured into this transparent growth container and left to solidify so that the glass slide was embedded in the hydrogel with a fixed tilt. *Medicago* seedlings were germinated until root growth was approximately 1 cm. They were then transplanted into the container allowing unobstructed vertically aligned growth until the root made contact with the glass slide. The *Medicago* plant was left to grow at room temperature with 12 hours of light per day. The roots were imaged once they reached a length of about 5-6 cm.

3D imaging setup and root reconstruction.

To acquire data for roots growing on inclined barriers where $\theta > 0°$, we used a 3D imaging system consisting of a fixed laser sheet and a translational stage enclosed in a light-controlled environment [24] (Fig. 1A of main text). Prior to imaging, the growth light is first turned off. The plant specimen, which is now under dark conditions, is translated along a linear axis through the laser sheet. While the plant moves through the plane of illumination, a digital camera acquires a series of images corresponding to each illuminated plane. This image stack is then saved for later analysis and 3D reconstruction with a voxel size of $0.1 \times 0.1 \times 0.2$ mm^3. Once image acquisition is completed, the stage resets to its initial position, and the growth light is returned to its prior state. Using MATLAB's morphological reconstruction toolbox, we are able to extract the centerline of the primary root from the raw image data with a spatial resolution of 0.3 mm (Fig. 2 of main text). For roots growing on a horizontal surface where $\theta = 0°$, we acquire image data by taking two dimensional (2D) photographs from beneath the transparent growth container. We then apply a thresholding filter to extract the centerline with a spatial resolution of 0.15 mm.

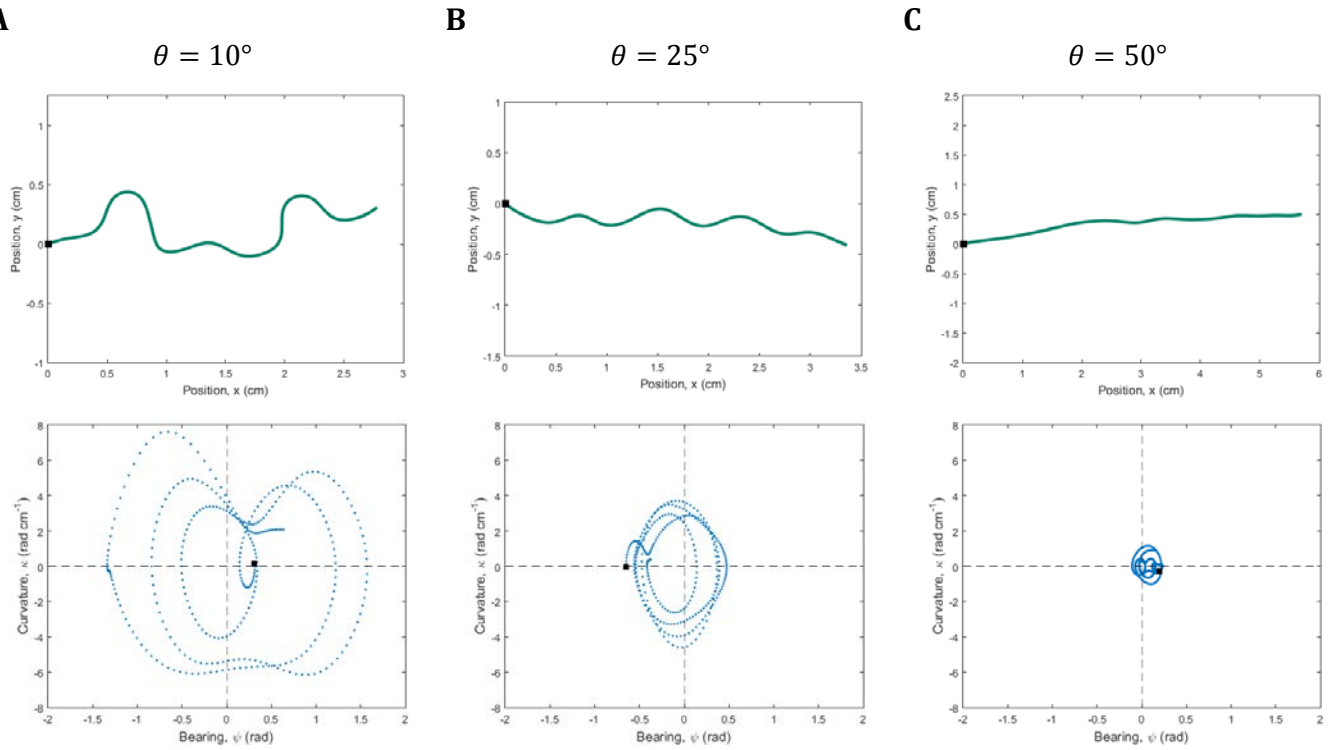

Fig. S1. Possible mathematical modeling using phase diagrams of root trajectories.

Phase diagrams of root trajectories provide a potential mathematical framework to quantitatively understand root behavior. By plotting $\frac{d\psi}{ds}$ versus $\psi(s)$ for 3 roots at $\theta = 10°$, $25°$ and $50°$ (*A*-*C*), we can follow the evolution of root curvature in phase space. The black square denotes the starting position of the root. To first order approximation, we observed that the phase trajectories eventually settle into a limiting ellipse. Therefore, we posit that the root trajectory follows the following ordinary differential equation:

$$C_1 \left(\frac{d\psi}{ds}\right)^2 + (\psi - \psi_0)^2 = C_2,$$

where ψ denotes the bearing, $\frac{d\psi}{ds}$ denotes the rate of change of bearing, and C_1, C_2, ψ_0 are parameters to be fitted. Geometrically, C_1 and C_2 characterize the wavelength and amplitude of root waving while ψ_0 characterizes the skewing angle. This approach removes the randomness in the switching mechanism, but is capable of quantifying the trend observed in root curvature at different tilt angle θ.

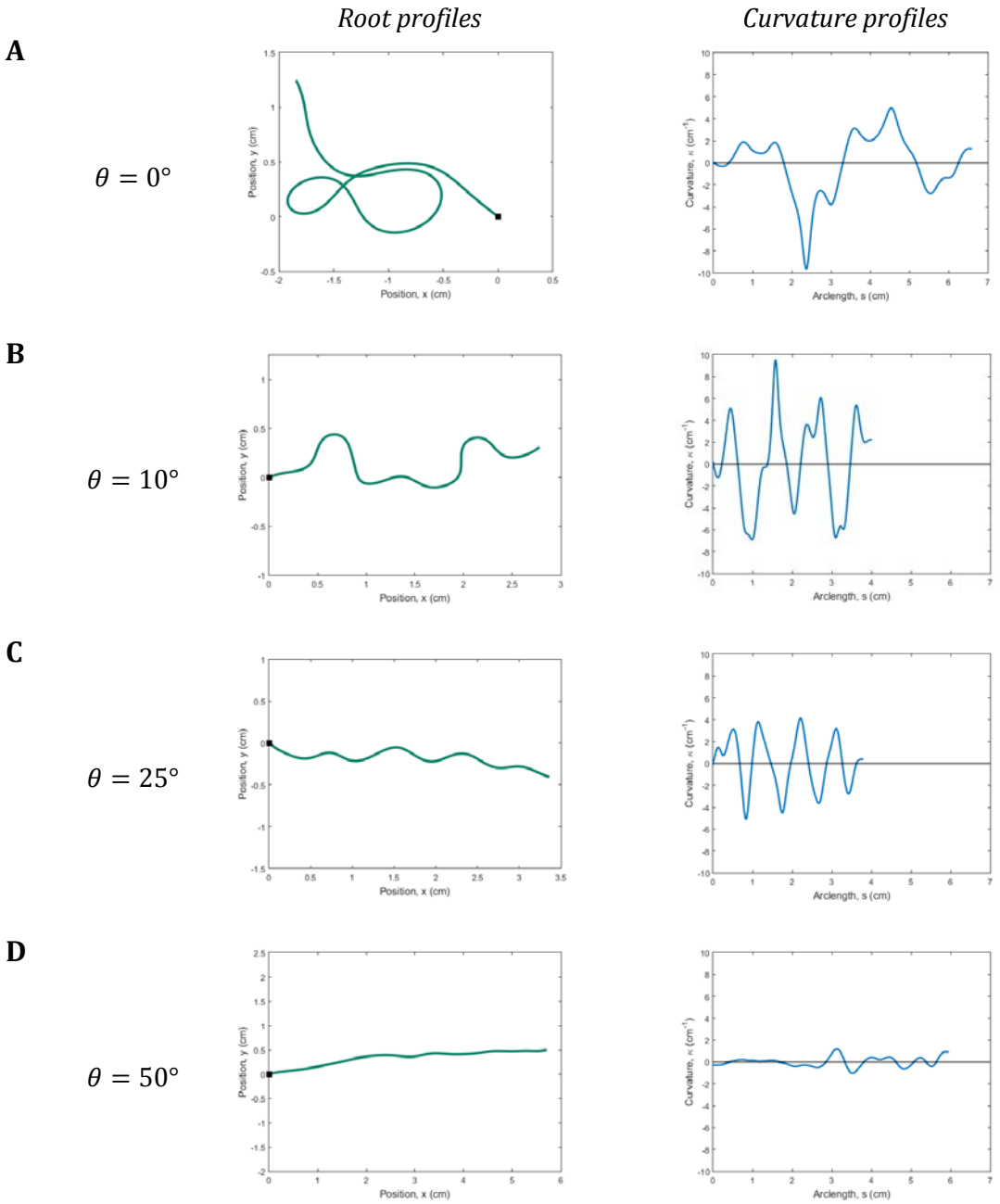

Fig. S2. curvature profiles $\kappa(s)$ of representative root samples.

Curvature profiles of four representative root samples. The curvature profiles of roots at different θ's (*A-D*) are plotted as a function of arclength s. The point where each root makes first contact with the tilted plane is marked with a black square.

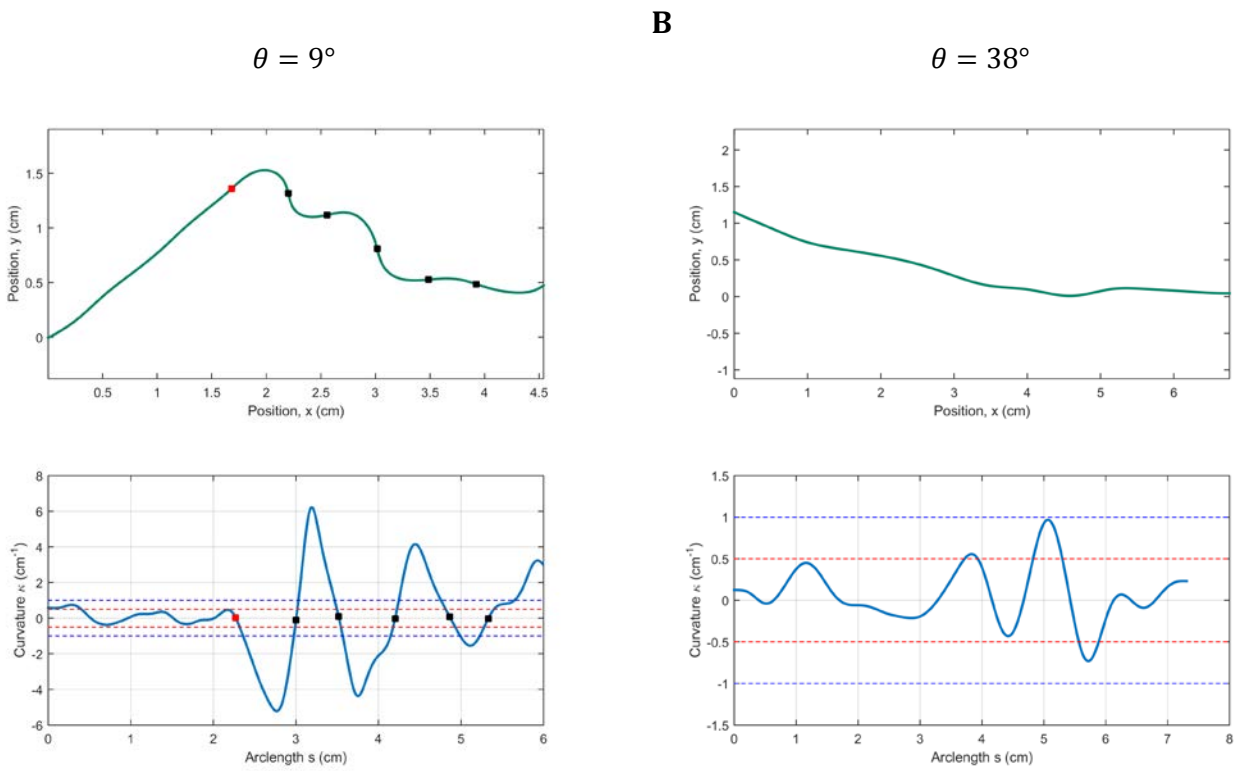

Fig. S3. Curvature resolution limit and threshold for defining s_0.

The resolution of our 3D imaging and reconstruction technique set a lower limit of 0.5 cm^{-1} on the curvature values that can be reliably measured (red dotted line, *A, B*). Moreover, samples that clearly demonstrate root waving show an initial period of nearly straight growth (Fig. 3A of main text, $s < s_0$). In order to eliminate this transient growth period from our analysis, we set a threshold of 1 cm^{-1} (blue dotted line, *A, B*) for all samples to define the point s_0 where root patterns begin to emerge. In the waving regime, as illustrated by a representative root at $\theta = 9°$ in (*A*), the first segment of root with curvature magnitude greater 1 cm^{-1} determines the onset of root waving (red square). In addition, we can reliably determine the switching points (black squares) because root segments have curvature magnitudes significantly greater than the resolution. However, in the skewing regime, as illustrated by a representative root at $\theta = 38°$ in (*B*), most segments have curvature values below that of our resolution and hence the switching points cannot be reliably determined. Of the 57 roots in the waving regime ($6° \leq \theta \leq 28°$), 9 roots are omitted from analyses that are dependent on reversal events because the root waving onset point s_0 cannot be determined. In the skewing regime ($30° < \theta$), 11 out of 22 roots do not have s_0 that can be reliably identified. Therefore, analyses that are dependent on reversal events are not performed on this group of roots. All roots in the coiling regime have an s_0 that can be readily determined.

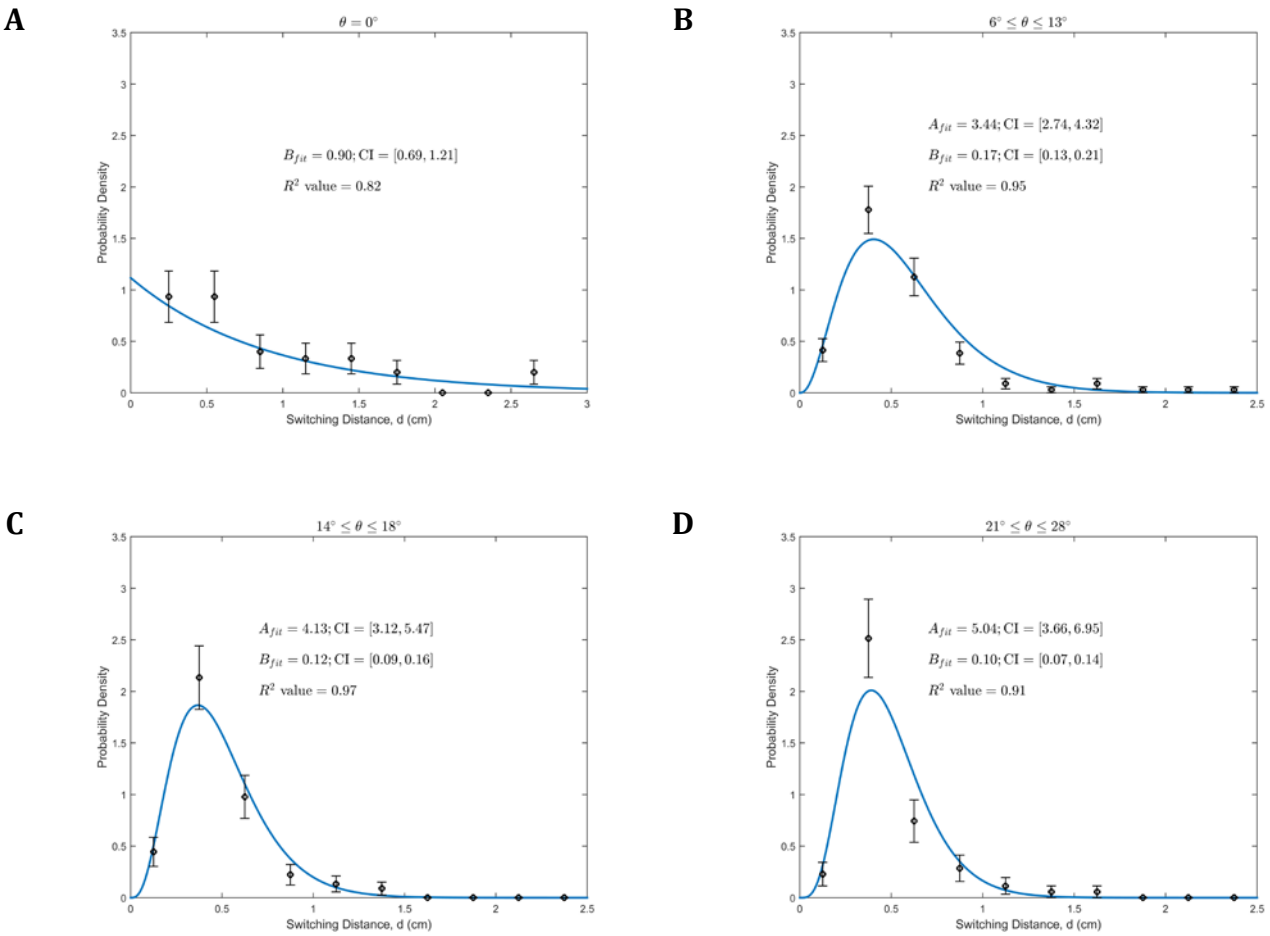

Fig. S4. Probability density of switching distance $P(d)$ using maximum likelihood estimation (MLE).

Probability distribution of switching distance $P(d)$ as a function of tilt angle θ fit to a gamma distribution (A-D). The gamma distribution is given by $P(d; A, B) = e^{-d/B} d^{A-1}/B^A \Gamma(A)$, where A is the shape parameter, and B is the scale parameter. The maximum likelihood estimation (MLE) of the parameters are stipulated in the respective plots. The 95% confidence interval for each parameter and the R^2 values are indicated as well. For the case of $\theta = 0$, we set $A = 1$ to simplify the gamma distribution to a Poisson distribution (negative exponential), which is known to arise in unbiased random walks.

In our analysis of the root switching distance data, we tested the log-normal and gamma distributions. While both had comparable fits with $R^2 > 0.9$ on tilted barriers, we find the gamma distribution offers a more insightful explanation of root coiling as a memoryless random process on horizontal barriers. Moreover, previous studies (see reference [33] and [34] of main text) studying *E. coli* motion in chemically uniform environments found a statistical distribution of run lengths well described by a Poisson distribution (i.e., gamma distribution with $A = 1$), which is analogous to the case of root growth on a horizontal barrier where we fit for the same function. Taken together, the insights and enhanced explanatory power of the gamma distribution motivate the analysis presented in the main text.

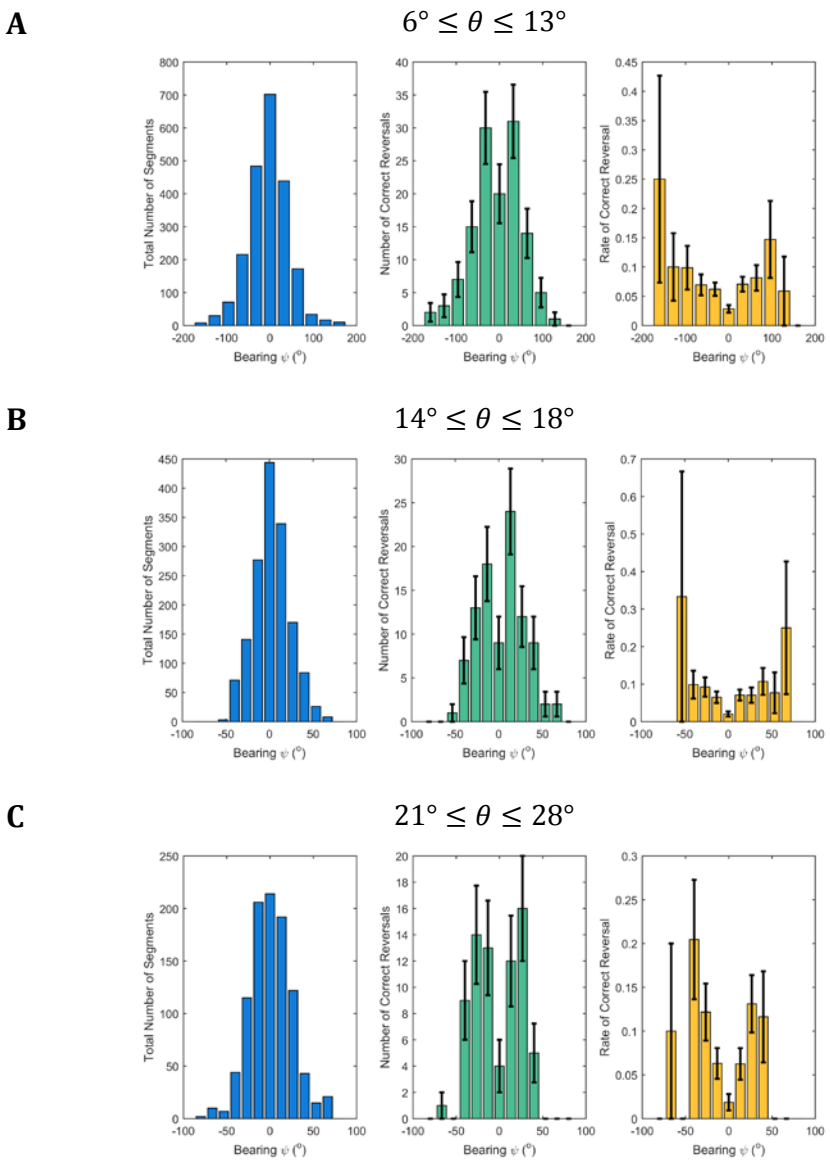

Fig. S5. Histogram of correct and incorrect reversals.

The rate of correct reversal is defined as the probability that an infinitesimal segment of root at a particular bearing ψ will reverse its chirality so that the subsequent root segments will bend in a more downhill direction (i.e. decreasing $|\psi|$, Fig. 5A of main text). To compute this reversal rate, we discretized the root into short segments of 0.04 cm long and binned them (blue, *A*-*C*). We then calculated the number of root segments within each bin that corresponded to correct reversal events (green, *A*-*C*). Dividing the number of correct reversals by the total number of segments, we obtained the rate of correct reversal (yellow, *A*-*C*). Due to "grow-and-switch" gravitropism, the rate of reversal graphs in the waving regime exhibit increasingly steeper 'V' shape curves as θ gets larger.

D $\theta = 0°$

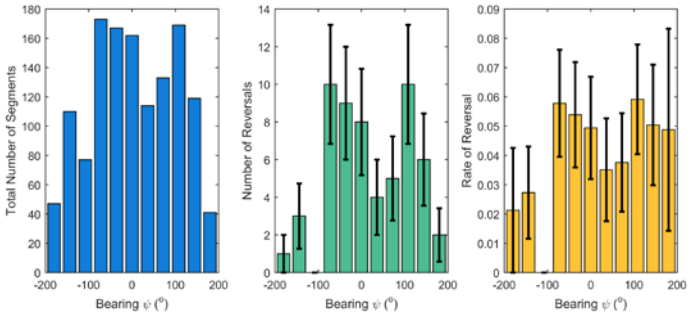

Fig. S5. Histogram of correct and incorrect reversals (continued).

Note that at $\theta = 0°$, the choice of $\psi = 0°$ is arbitrary and reversal events are neither correct nor incorrect, since there is no gravitational gradient. A similar analysis is performed to the data and the rate of reversal shows uniform distribution (D), consistent with expectations based on *E. coli* 's behavior in a chemically isotropic environment. To exclude outlier reversals, we do not include any data point with n=1 for analysis in Fig. 5B of main text.

E $6° \leq \theta \leq 13°$

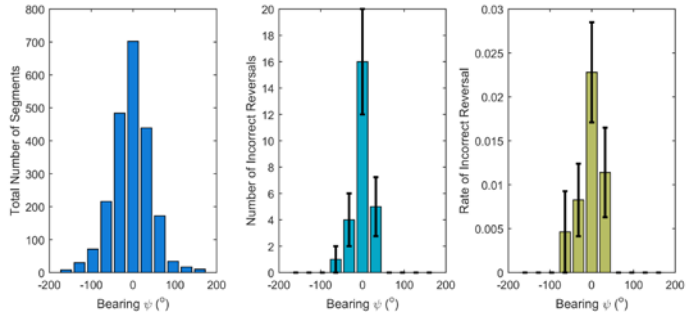

F $14° \leq \theta \leq 18°$

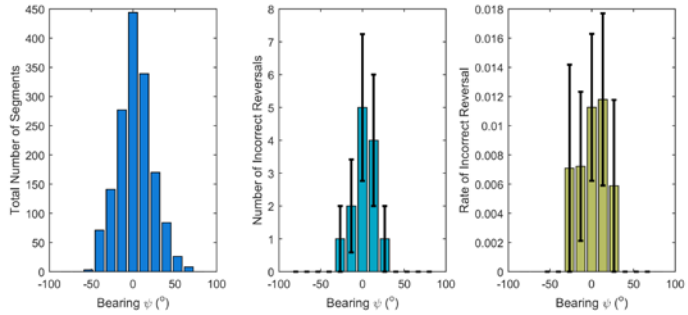

G $21° \leq \theta \leq 28°$

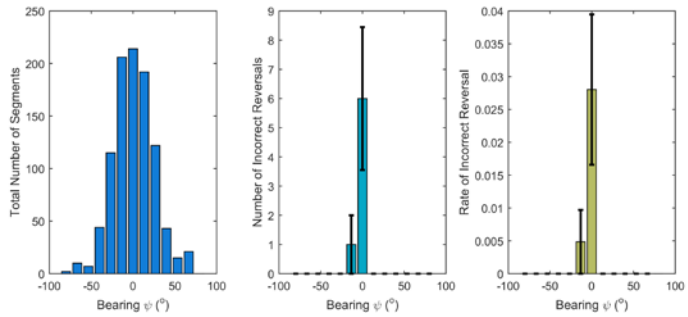

Fig. S5. Histogram of correct and incorrect reversals (continued).

Analogous to *(A-C).*, the rate of incorrect reversal is defined as the probability that an infinitesimal segment of root at a particular bearing ψ will reverse its chirality so that the subsequent root segments will bend in a less downhill direction (i.e. increasing $|\psi|$, Fig. 5A of main text). To compute this reversal rate, we discretized the root into short segments of 0.04 cm long and binned them (blue, *E-G*). We then calculated the number of root segments within each bin that corresponded to an incorrect reversal event (cyan, *E-G*). Dividing the number of incorrect reversal event by the total number of segments, we obtained the rate of wrong reversal (dark yellow, *E-G*). We observe that the incorrect reversal rate is centered at $\psi = 0°$ and the distribution gets narrower with increasing θ. This is consistent with the notion that the root is better able to find the downhill direction at large θ with less incorrect reversal.